Acta Materialia 270 (2024) 119839

Contents lists available at ScienceDirect

Acta Materialia

journal homepage: www.elsevier.com/locate/actamat

Full length article

Combinatorial and high-throughput investigation of growth nanotwin formation

A. Alwen [a], A. Liang [a], P.S. Branicio [a], A.M. Hodge [a,b,*]

[a] Mork Family Department of Chemical Engineering and Materials Science, University of Southern California, Los Angeles, CA 90089, USA
[b] Department of Aerospace and Mechanical Engineering, University of Southern California, Los Angeles, CA 90089, USA

ARTICLE INFO

Keywords:
Nanotwin
Combinatorial
High-throughput
Sputtering

ABSTRACT

This study examines the synthesis of growth nanotwins in CuNi alloys using combinatorial and high-throughput experimental techniques. 338 unique CuNi samples were synthesized via co-sputtering to create a material library encompassing composition, hardness, phase, and crystallographic data. The material library data in conjunction with scanning transmission electron microscopy was used to evaluate growth twinning over a wide compositional range (Cu – 6.8 to 58.8 at% Ni). A direct correlation between measured twin boundary spacings and the stacking fault energies underscored limitations of the current growth twin model caused by an underestimation of the free energy penalty for forming non-twinned grains. To address this, a refined model was developed to accurately capture the variation in twin boundary spacing and formation across all compositions. This model paves the way for high-throughput investigations into nanotwin synthesis in various alloy systems.

1. Introduction

Nanoscale twin boundaries (TBs), referred to as nanotwins (NTs), are important microstructural features that can be achieved via plastic deformation, annealing, and film synthesis techniques [1–8]. However, the latter (known as growth twinning) has rarely been explored for NTs, despite offering a wide compositional workspace and the greatest microstructural control. This is due to two main reasons: 1) the high experimental time costs to evaluate the wide synthesis space, and 2) the finite number of known material stacking fault energies (SFEs) [9–11]. SFEs are intrinsic material properties linked with growth TB formation that are not well documented because they can vary unpredictably with changing composition and are difficult and time intensive to measure (requiring detailed TEM characterization of dislocations or XRD peak shifting analysis) [1,9–15]. Computational techniques including molecular statics (MS) and density functional theory (DFT) have been employed as viable tools to estimate SFEs, but they still require experimental verification [16–19]. One route to overcome the SFE bottleneck is by augmenting computational approaches with combinatorial and high-throughput (CHT) experimental techniques to evaluate growth twinning across large compositional spaces. Recently, CHT materials research has emerged as a promising methodology to more efficiently discover and study materials, as it examines entire composition domains instead of being restricted to discrete points [20,21]. This approach leverages compositional gradients and high-throughput characterization techniques to generate large material property databases, known as material libraries, by analyzing hundreds or even thousands of samples in a single experiment [20,22–24]. Material libraries have been used to elucidate trends and explain phenomena for a range of material characteristics such as phase, crystal structure, and electronic and mechanical properties [21,22,25,26]. For example, Kube et al. used the data from their CHT study to identify new phase selection criteria with respect to changing composition for high entropy alloys [22]. While the large datasets from CHT studies have been successful in analyzing the aforementioned material characteristics, the impact and applicability of CHT techniques can be broadened by expanding the use of material library data to study microstructural and intrinsic material phenomena, such as growth NTs and SFEs.

In the case of growth NTs, studies have been limited by the small number of materials with known SFEs, thus, CHT material libraries can provide large datasets that can be used to establish a more direct understanding of the links between SFE, composition, and TB formation [9, 27–29]. Growth twinning typically occurs during non-equilibrium film synthesis processes and it has been demonstrated that TB formation can

* Corresponding author at: Mork Family Department of Chemical Engineering and Materials Science, University of Southern California, 925 Bloom Walk, HED 216, Los Angeles, CA 90089, USA.
E-mail address: ahodge@usc.edu (A.M. Hodge).

https://doi.org/10.1016/j.actamat.2024.119839
Received 28 December 2023; Received in revised form 9 March 2024; Accepted 18 March 2024
Available online 19 March 2024

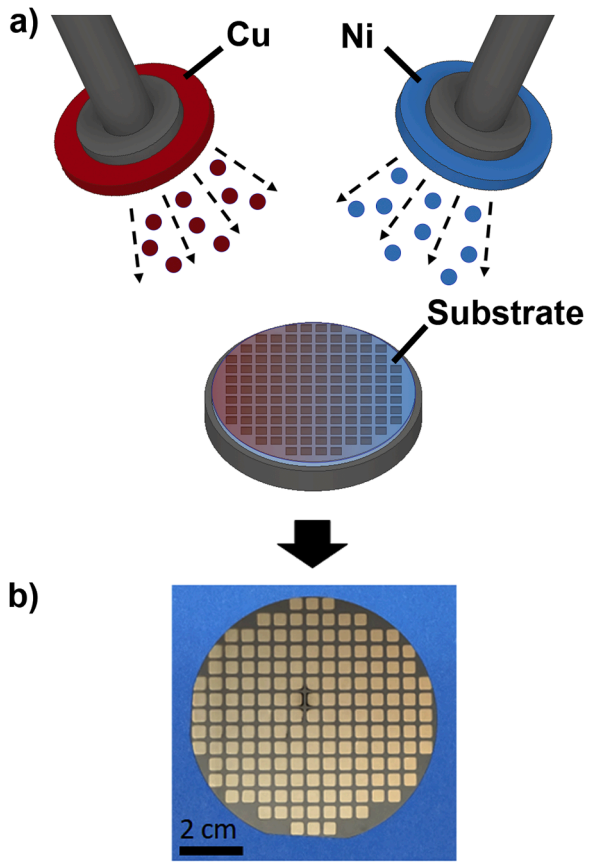

Fig. 1. Schematic of the combinatorial synthesis process. (a) Illustration of the co-sputtering technique, where two materials (Cu and Ni) are simultaneously deposited to form a compositional gradient. (b) Image showing a combinatorial array of co-sputtered samples deposited on a 10 cm wafer, where each 5 × 5 mm square represents a unique CuNi sample.

be influenced by synthesis and material parameters, including the deposition rate, temperature, and SFE [1,30]. Given these relationships, current research has utilized magnetron sputtering to investigate growth NTs because it couples control of growth TB formation with a wide compositional workspace. This has been used to examine NT formation in single-element and multi-element alloys such as Ag, Cu, stainless steels, and HEAs [4,5,27,31–34]. For the few materials with experimentally characterized SFE's, it has been observed that materials with lower SFEs (SFE $\leq$ 50 mJ m^{-2}) tend to have greater rates of growth NT formation than higher SFE materials (SFE $\geq$ 120 mJ m^{-2}) [4,9,28,35]. To capture this relationship, Zhang et al. developed a thermodynamic model that utilizes known SFEs and deposition parameters to estimate the resulting growth TB spacings; however, this model is restricted to order of magnitude approximations for low SFE materials due to limited data, which hinders its ability to predict TB formation in other material systems [4,35]. Therefore, growth twinning presents a model system to investigate and establish novel approaches to analyze material library data, amplifying the impact of CHT research.

In this work, a high-throughput experimental approach to examine NT synthesis domains is demonstrated using the CuNi alloy system. Combinatorial co-sputtering was employed to synthesize 338 CuNi samples with compositions ranging from Cu – 6.8 at% Ni to Cu – 58.8 at % Ni. Following synthesis, high-throughput characterization techniques, including X-ray diffraction (XRD), scanning electron microscopy (SEM), and nanoindentation were used to generate material libraries to analyze structural, morphological, and mechanical properties. Additionally, cross-sectional microstructures of representative CuNi samples were examined via scanning transmission electron microscopy (STEM) to elucidate relationships between composition and NT formation. The observed microstructural trends were then compared with CuNi SFEs estimated using MS calculations. Overall, the combination of CHT techniques and in-depth analysis in this study provides new insights into growth NT formation leading to a revised growth twinning thermodynamic model, ultimately demonstrating a novel path to analyze intrinsic and microstructural material properties.

2. Experimental methods

CuNi compositional libraries were synthesized via combinatorial co-sputtering, with two sources used to deposit Cu (99.999 %) and Ni (99.995 %) from 5.08 cm diameter targets (Plasmaterials) onto two stationary 10 cm Si (100) substrates at a base pressure of 5 × 10^{-4} mTorr, sputtering pressure of 5 mTorr, a source to substrate working distance of 14 cm, and cumulative deposition rate of 1.2 nm s^{-1}. As shown in Fig. 1, the material deposited onto each wafer was divided using a mask into 169 5 × 5 mm alloy sections, resulting in 338 unique CuNi samples. The average sample thickness was 2 μm and thicknesses ranged from 1.1 μm - 2.3 μm depending on location due to deposition on the stationary substrate. A total compositional range of Cu – 6.8 at% Ni to Cu – 58.8 at% Ni was achieved by altering the sputtering power to the Cu and Ni targets when depositing onto each substrate. Within a given square, composition was observed to vary by up to +/- 1.7 at% Ni when measuring across a 4 mm distance. Characterization and analysis was performed in the middle of each square (with a tolerance of 0.5 mm) to limit compositional variation to less than ~0.2 at% Ni. For the first wafer, the Cu and Ni targets were sputtered at 500 W and 155 W, respectively, while for the second wafer Cu was sputtered at 350 W and Ni was sputtered at 300 W.

High-throughput characterization techniques including energy dispersive X-ray spectroscopy (EDX), SEM, XRD, and nanoindentation were performed to analyze the composition, top surface morphology, crystal structure and phase, and mechanical properties of each CuNi sample, respectively. Composition and top surface morphology were characterized using the EDX and SEM capabilities of a Helios G4 PFIB UXe DualBeam FIB/SEM and Zeiss Gemeni II SEM. SEM images were taken at a 10 kV accelerating voltage, 0.8 nA current, and 4.0 mm working distance in the Helios SEM and 5 kV accelerating voltage, 1.0 nA current, and 5.0 mm working distance in the Zeiss SEM. Both microscopes were equipped with the Oxford Instruments Aztec software, which was used to acquire EDX spectra for each CuNi sample using a 500,000 count limit, 5.5 mm working distance, and accelerating voltage and current of 20 kV, 0.8nA (Helios) or 15 kV, 1.0 nA (Zeiss). For analysis of the phase and crystal structure, XRD spectra were collected with an Empyrean Panalytical X-ray diffractometer. To characterize multiple samples in a single XRD session, an automated and programmable stage was used to center the incident X-rays on each 5 × 5 mm sample (XY position) and a laser sensor was used to identify and adjust the sample height (Z position). The incident X-rays were collimated to probe an area of roughly 4 × 4 mm to ensure that only a single composition was analyzed during each scan. Scans were performed using CuKα radiation with a 2θ range from 30° - 110°, a step size of 0.026°, and rate of 0.3 s per step. The rate and step size were chosen to yield six or more measurements above the full-width half maximum (FWHM) for each intensity peak. Hardness values for 64 selected CuNi samples from each wafer were measured using a Hysitron Triboindenter with a 100 nm Berkovich tip. A set of 12 indents, positioned 12.5 μm apart was performed in the center of each sample with a force-controlled, constant load rate, triangle load function, and decreasing maximum load from 3000 μN - 1000 μN. The indentation parameters were selected to ensure that the maximum indentation depth was 200 nm or less than 10 % the average sample thickness. The equation to calculate hardness is provided below in Eq. (1), where H is the hardness, P_{max} is the max load, and A is the contact area [36].

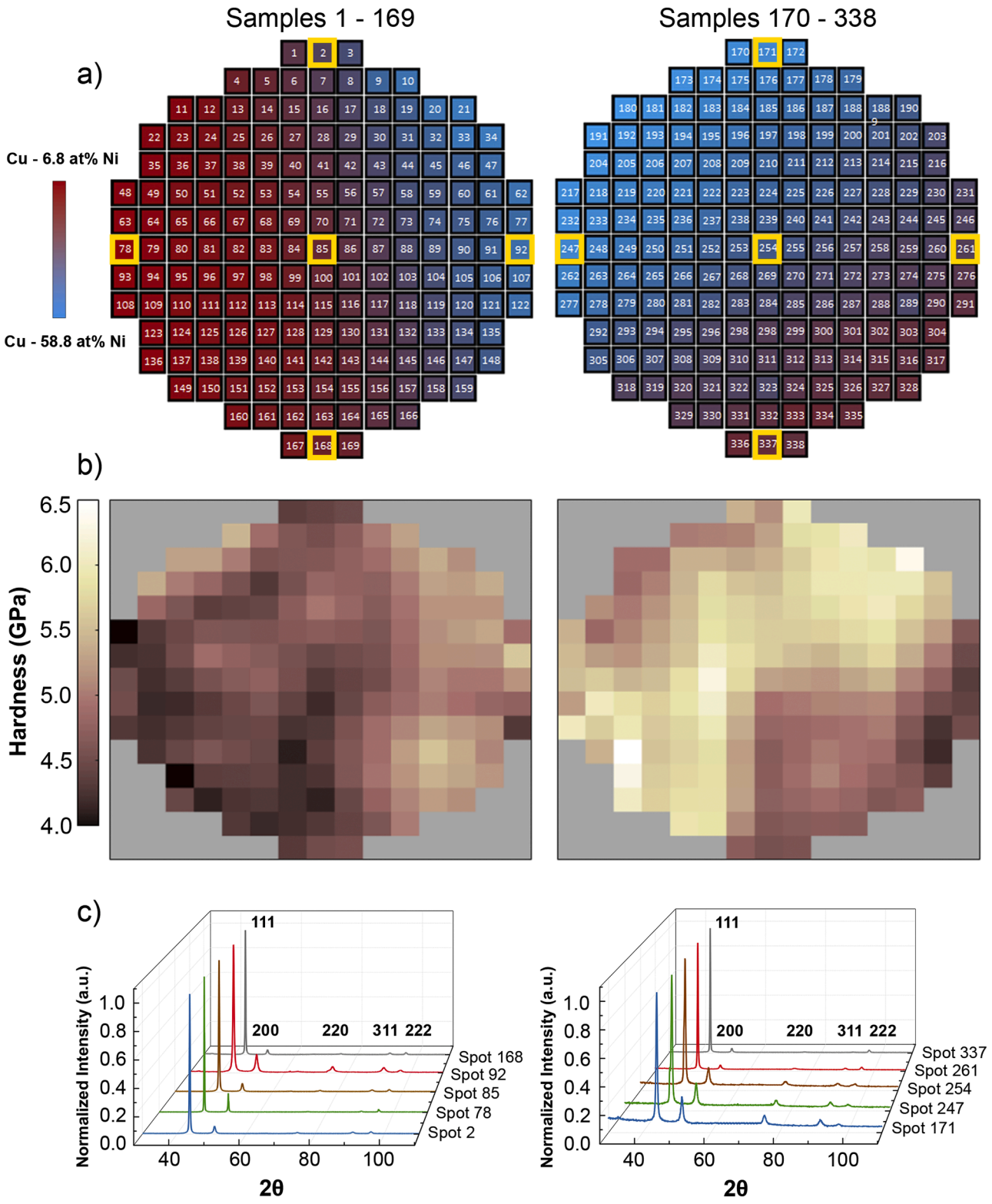

Fig. 2. Analysis of CuNi combinatorial samples. (a) Compositional maps obtained via EDX for two sets of combinatorial wafers, with the first wafer (samples 1–169) containing samples with compositions ranging from Cu – 6.8 at% Ni to Cu – 35.5 at% Ni and the second wafer (samples 170–338) containing samples with compositions ranging from Cu – 12.5 at% Ni to Cu – 58.8 at% Ni. (b) Corresponding hardness heat maps for the two wafers, where hardness values were measured using high-throughput nanoindentation. (c) Selected XRD patterns from the samples with yellow borders in 2a. (For interpretation of the references to colour in this figure legend, the reader is referred to the web version of this article.)

$$H = \frac{P_{max}}{A} \quad (1)$$

To generate hardness heat maps, the hardness values from the selected samples were input into a MATLAB code that used interpolation to estimate the hardness values for the remaining 105 samples.

Following high-throughput characterization, NT formation was analyzed in selected samples via STEM with a FEI Talos F200C G2 TEM at a 200 KeV accelerating voltage. TEM lamellae were prepared in the Helios G4 PFIB UXe DualBeam FIB/SEM using the plasma focused ion beam (PFIB) lift-out technique [37]. ImageJ software was used to determine the average TB spacing and percentage of NT grains observed in the sample cross-sections, where a NT grain was defined as a grain with the majority of its area containing TBs spaced less than 100 nm apart. TB spacing was calculated by measuring 100 TB per sample, while the percentage of NT grains was determined by counting how many grains out of a set of 100 were nanotwinned. The experimentally measured NT formation was compared with theoretically predicted TB spacings calculated from SFEs obtained via MS calculations with the LAMMPS software. The MS SFE calculations were performed over a compositional range from Cu – 0 at% Ni to Cu – 75 at% Ni. First, pure face-centered cubic (FCC) Cu systems, oriented along the ⟨112⟩, ⟨111⟩, and ⟨110⟩ crystallographic directions–corresponding to the *x, y*, and *z* directions– were constructed with a simulation cell of dimensions 355 × 205 × 125 Å^3. This system comprised 80 × 80 × 40 lattice cells along each direction. The dimensions were carefully chosen to minimize the influence of local composition variations on the gliding plane and to lessen the free surface effects along the ⟨110⟩ direction. Please see Figs. S1(a) and (b) for the convergence tests of the gliding plane area and thickness along the ⟨110⟩ direction. Alloy systems for each desired composition were then created by randomly substituting certain amounts of Cu with Ni atoms, followed by energy minimization to allow the system to reach equilibrium. Periodic boundary conditions were applied in all three dimensions and a 10 Å vacuum separation layer was introduced at the top and bottom to preclude periodic image interactions. Stacking faults were generated by displacing the upper half of the simulation box along the ⟨112⟩ direction, which represents the most energetically favored slip system for FCC metals. While the system was displaced, the atoms were allowed to relax along the direction perpendicular to the stacking fault plane. Figures S1(c) and (d) provide a visual representation of the local structure before and after the creation of the stacking fault. The SFE, γ_{SF}, was calculated using Eq. (2), where E_i and E_f are the system energies before and after the creation of the stacking fault, and A is the gliding plane area [19]. An Embedded Atom Model (EAM) potential was used for Cu-Ni interactions, recognized for its satisfactory accuracy in modeling the mechanical properties of alloy systems under various conditions, including radiation damage, tensile and shock loading, and nanoindentation [38–41]. The LAMMPS software was used to conduct all molecular statics calculations and OVITO was used in visualization and local structural analysis [42,43].

$$\gamma_{SF} = \frac{E_f - E_i}{A} \quad (2)$$

3. Results and discussion

As described in the background, material library datasets can be leveraged to analyze microstructural features and intrinsic material properties. Thus, to demonstrate a high-throughput approach to investigate NT synthesis domains, the CuNi alloy system was selected as an ideal candidate because Cu is a low SFE material (~ 40 mJ m^{-2}), Ni is a high SFE material (~120 mJ m^{-2}), and adding Ni solute to Cu increases the SFE, unlike many alloys where SFE can vary unpredictably with composition [44,45]. Additionally, Cu and Ni tend to form solid

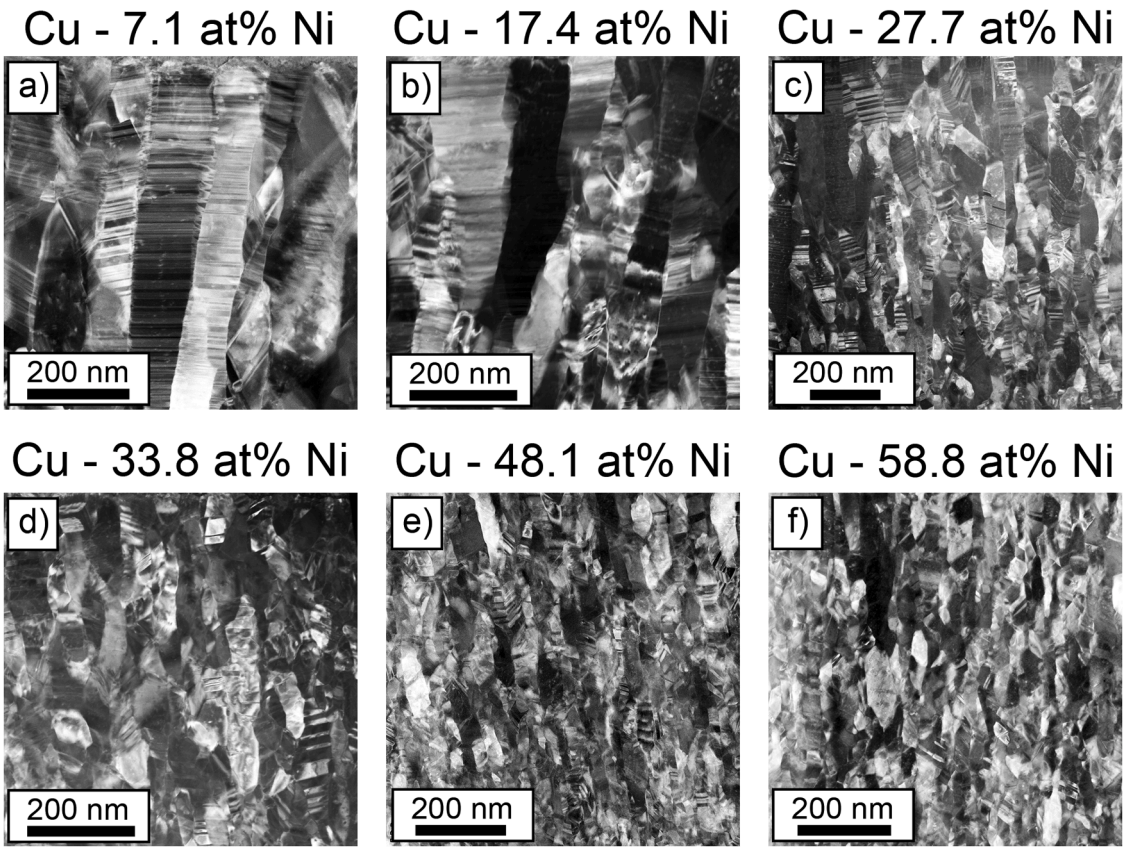

Fig. 3. Cross-sectional HAADF STEM micrographs for selected CuNi samples highlighting the change in growth nanotwin formation as Ni concentration increases from (a) 7.1 at% Ni to (f) 58.8 at% Ni.

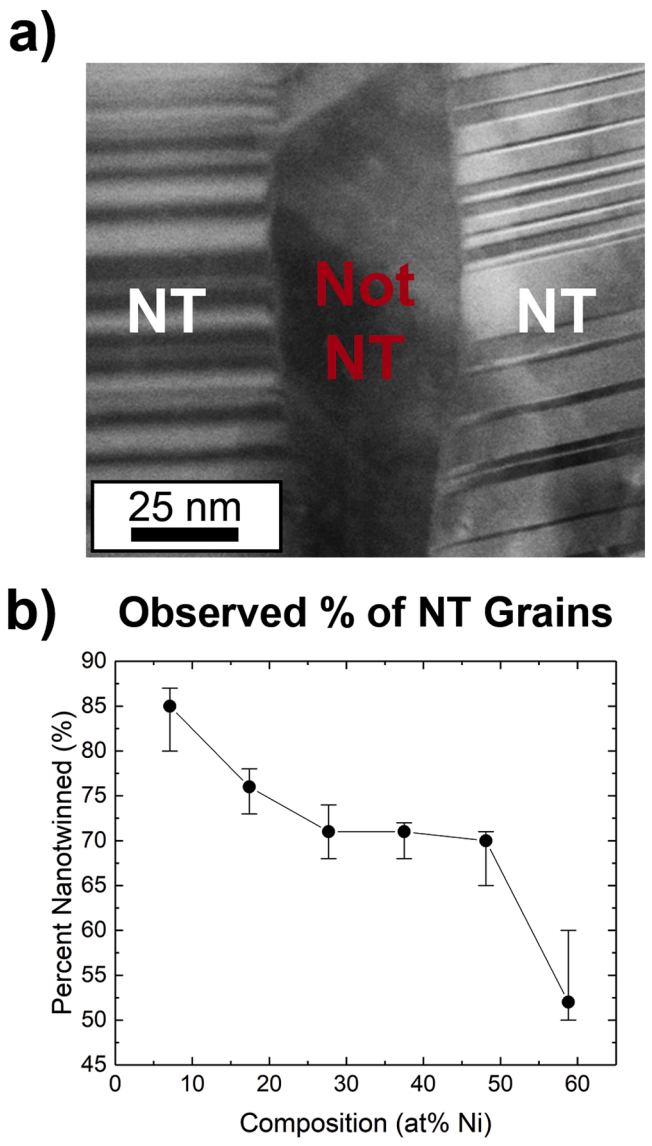

Fig. 4. Nanotwin formation in CuNi alloys and quantitative assessment. (a) STEM micrograph comparing nanotwinned (NT) and non-nanotwinned (Not NT) grains. A nanotwinned grain is defined as a grain with the majority of its area containing twin boundaries spaced ≤ 100 nm apart. (b) Plotted comparison of the quantified percentage of NT grains relative to the total observed grains, as a function of Ni concentration.

solutions, so NT formation should not be influenced by secondary phases and/or intermetallics, which could complicate analysis of twin nucleation [46,47]. As a result, this material system can be studied and used to create foundational approaches to link CHT libraries with NTs and other material phenomena.

3.1. Analysis of material libraries

In order to identify composition-property trends in the material libraries that could be linked with NT formation, detailed property maps, shown in Fig. 2, were created to summarize the compositional, mechanical, and structural data collected via high-throughput EDX, nanoindentation, and XRD. Fig. 2a highlights the CuNi compositional gradients for the two combinatorial wafers, spanning from Cu – 6.8 at% Ni to Cu – 58.8 at% Ni, where the areas in red and blue indicate samples with greater Cu or Ni concentrations, respectively, and the yellow borders identify selected samples that will be further discussed in Fig. 2c. For quick identification, the samples on each wafer were labeled numerically from left to right, with the first wafer containing samples 1–169, which ranged from Cu – 6.8 at% Ni to Cu 35.5 at% Ni, while the second wafer contained samples 170–338, which ranged from Cu – 12.5 at% Ni to Cu – 58.8 at% Ni. The overlap in sample compositions from Cu – 12.5 at% Ni to Cu – 35.5 at% Ni was used to check and verify material property measurements. It was observed that the Ni concentration of neighboring samples varied by ± 1 to 5 at.% Ni depending on the distance from the Cu and Ni sputtering targets, with the larger compositional changes observed in the middle of the wafer. Complementing the compositional analysis, CuNi hardness values were then mapped for each wafer, as seen in Fig. 2b, and compared to the composition map in Fig. 2a. From these maps it can be seen that the CuNi alloy hardness increases with greater Ni content, likely due to solid solution strengthening and Ni's higher yield strength ($\sigma_{ys,\ Ni}$ = 138 MPa, $\sigma_{ys,Cu}$ = 69 MPa) [46,48]. However, there were also variations in hardness that indicate other strengthening mechanisms, such as Hall-Petch strengthening, are affecting the CuNi alloy mechanical properties [49]. To further develop the CuNi material libraries, the structural properties of the CuNi alloys were analyzed via SEM and XRD to determine how the top surface morphology, texture, or phase could be affecting the resulting material properties. High-throughput SEM imaging revealed minimal change in top surface morphology with respect to varying composition, as shown in Figure S2 in the Supplementary Materials, which displays the top surface morphologies for six compositionally unique representative CuNi samples. From the XRD analysis, it was determined that all CuNi samples achieved a single-phase solid solution, with an FCC crystal structure and strong (111) texturing. A small change in the ratio of (111) to (200) peak intensities was observed, which was not dependent on composition or location within the array of combinatorial samples. However, given the strong (111) texturing in all samples, this variation in (200) peak intensity is not expected to significantly influence the CuNi material properties. An example of the XRD data is highlighted in Fig. 2c, which displays selected XRD diffractograms from the samples with yellow borders mapped in Fig. 2a; these samples were chosen as they represent the entire composition range and are located at distinct positions on each wafer. Overall, the material library data highlights that CuNi is an ideal system to investigate growth NT's because there are no other phases, morphologies, or textures present affecting the microstructure or material properties, which enables a down selection from the entire compositional array to representative samples that evaluate NT formation or the lack thereof.

Table 1
Composition, nanotwin formation, grain width, and hardness data for selected CuNi samples characterized via STEM, ImageJ, and nanoindentation.

Composition	NT Percentage (%)	Grain Width (nm)	Twin Spacing (nm)	Hardness (GPa)
Cu - 7.1 at% Ni	84 %	84.8	4.4	4.5
Cu - 17.4 at% Ni	76 %	65.9	7.2	4.4
Cu - 27.7 at% Ni	71 %	56.5	7.8	5.5
Cu - 33.8 at% Ni	71 %	40.3	9.4	5.1
Cu - 48.1 at% Ni	70 %	47.2	10.6	5.0
Cu - 58.8 at% Ni	52 %	39.9	16.9	4.9

3.2. Analysis of NT formation

To study growth NT formation as a function of composition, representative samples were examined using STEM at approximately 10 at% Ni concentration intervals, with the resulting analysis presented in Figs. 3 and 4 and summarized in Table 1. Fig. 3 shows the cross-sectional STEM micrographs for the six selected CuNi samples, which had compositions of Cu – 7.1 at% Ni (3a), Cu – 17.4 at% Ni (3b), Cu – 27.7 at% Ni (3c), Cu – 33.8 at% Ni (3d), Cu – 48.1 at% Ni (3e) and Cu – 58.8 at% Ni (3f). From the STEM images, it can be seen that increasing Ni content influences NT formation in grains, the columnar grain widths, and the overall TB spacings. With respect to NT formation in grains, Fig. 4 depicts examples of NT and non-NT grains (4a) and a plot of the decrease in the percentage of NT grains in each CuNi sample from 84 % NT (Cu – 7.1 at% Ni) to 52 % NT (Cu – 58.8 at% Ni) as a function of increasing Ni concentration (4b). A similar trend has been observed in previous studies, although at higher Ni concentrations (~10 at% Ni or greater) NTs were not expected since greater Ni content increases the SFE [4,9,19,28,35]. Table 1 shows a detailed summary of the measured percentages of NT grains, columnar grain widths, TB spacings, and hardness values for the respective alloys, and, from this table, it is observed that higher Ni content also yields a decrease in the columnar grain width and an increase in the TB spacing. These varying microstructural features can directly influence a wide range of material properties, such as the alloy's resulting conductivity, thermal stability, or hardness [1,5,6]. Specifically, in regard to the nanoindentation maps (Fig. 2b) changes in NT formation and columnar grain width impact CuNi hardness by inversely affecting Hall-Petch strengthening (see Table 1), where the hardness initially increases, due to the smaller grain width, and then decreases due to the reduced NT formation. Further analysis can be found in the Supplementary Materials section in Figure S3, noting that the overall changes in hardness can be accounted for by the aforementioned mechanisms and compositional variations [48,49].

From Table 1, it is noted that the percentage of NT grains and the TB spacing change as a function of the Ni concentration. For TB spacing specifically, the minimal increase from 4.4 nm (Cu – 7.1 at% Ni) to 16.9 nm (Cu – 58.8 at% Ni) largely deviates from the theoretical predictions of the model developed by Zhang et al. where, due to the increase in SFE, the TB spacing would be expected to increase orders of magnitude [4]. Thus, the presence of NTs in all samples examined in this study (with concentrations as high as Cu – 58 at% Ni) highlights a disconnect in the current model, limiting its ability to predict growth twinning over large composition and SFE ranges.

3.3. Revised growth twinning model

Using the CuNi material library data presented herein, a revised thermodynamic model can be developed to better understand growth twin nucleation during sputtering. First, NT formation must be evaluated as a function of a generalized material parameter that influences TB spacing, namely the SFE, which changes as a function of composition. The use of SFE to calculate growth TB spacing is presented in the original thermodynamic model by Zhang et al., which is shown in Eq. (3) [4,28].

$$\lambda = \left[\exp\left(\frac{\pi\gamma^2 h y_{twin}}{kT\Delta G_v(h\Delta G_v - \gamma_{twin})}\right)\right]h \tag{3}$$

Here, λ is the TB spacing, h is the height of the columnar grain (assumed to equal the (111) interplanar spacing), ΔG_v is the bulk free energy per unit volume, k is Boltzman's constant, T is the temperature, γ is the surface energy, and γ_{twin} is the twin boundary energy, which is approximately equal to half the SFE ($\gamma_{twin} \approx SFE/2$) [4,28]. Surface energy, γ, was assumed to change with composition following the rule of mixtures. Thus, the surface energy will equal $(\gamma_{Cu})x + (\gamma_{Ni})(1\text{-}x)$, where $\gamma_{Cu}$and γ_{Ni} are the surface energies of pure Cu and Ni (1.185 J m^{-2} and 1.606 J m^{-2} respectively) and x is the atomic fraction of Cu in the alloy [50,51]. The bulk free energy per unit volume for a gas-solid transformation, ΔG_v, is calculated using Eqs. (4) and (5), where Ω is the atomic volume, P_v is the super saturated vapor pressure, P_s is the vapor pressure above the solid, m is the atomic mass of the deposited material, and J is the deposition flux [4].

$$\Delta G_v = \frac{kT}{\Omega}\ln\left(\frac{P_v}{P_s}\right) \tag{4}$$

$$J = \frac{P_v}{\sqrt{2\pi mkT}} \tag{5}$$

The growth twinning model determines TB spacing using the ratio of nucleation rates between "perfect" and "twinned" columnar grains ($I_{perfect}$ and I_{twin}) highlighted below in Eq. (6) [4].

$$\ln\left(\frac{I_{perfect}}{I_{twin}}\right) = -\frac{\Delta G^*_{perfect}}{kT} + \frac{\Delta G^*_{twin}}{kT} \tag{6}$$

$\Delta G^*_{perfect}$ and ΔG^*_{twin} are the critical free energies for the "perfect" and "twinned" nucleating columnar grains, respectively. These variables are calculated using the change in total free energy associated with forming each type of grain, which are shown in Eqs. (7) and (8), and are related to the variables in Eq. (6) through the critical radius [4].

$$\Delta G_{perfect} = 2\pi rh\gamma - \pi r^2 h\Delta G_v \tag{7}$$

$$\Delta G_{twin} = 2\pi rh\gamma - \pi r^2 h\Delta G_v + \pi r^2\gamma_{twin} \tag{8}$$

In the model, the shape of the columnar grain growth is assumed to be cylindrical, where Eq. (8) includes an additional energy term for the TB at the top surface of the nucleating grain ($\pi r^2\gamma_{twin}$) [4]. This energy factor leads to the lower calculated rates for "twinned" grain formation as compared to "perfect" grains. Specifically, it is assumed that there is no surface energy penalty on the top surface of a "perfect" grain during nucleation, but this implicit assumption leads to the model's exponential increase in predicted TB spacings. To account for this energy contribution, a factor for the surface energy at the top of the "perfect" columnar grain, γ_{top}, must be added to Eq. (7), which leads to Eq. (9).

$$\Delta G_{perfect} = 2\pi rh\gamma - \pi r^2 h\Delta G_v + \pi r^2\gamma_{top} \tag{9}$$

However, it is still more energetically favorable to form a "perfect" grain over a grain with a TB defect, thus the following can be assumed:

$$\gamma_{top} < \gamma_{twin} \tag{10}$$

and

$$z = \gamma_{twin}/\gamma_{top} > 1 \tag{11}$$

In Eq. (11), because the TB energy is greater than the top surface energy of a "perfect" grain, z must be greater than 1. γ_{top} is a distinct material value from γ, since the latter is defined to be the surface energy for the round side wall of the nucleating disc/cylinder that interacts with adjacent grains, while the former is for the top surface, which interacts with the vacuum environment during deposition. Using Eq. (9) and the relationship between the TB and top surface energies in Eq. (11), an updated predictive model is derived below.

$$\lambda = h\left[\exp\left(\frac{\pi\gamma^2 h y_{twin}}{kT\left(\Delta G_v - \frac{\gamma_{top}}{h}\right)(h\Delta G_v - \gamma_{twin})}\right)\right]^{(1-1/z)} \tag{12}$$

A key difference between the updated model in Eq. (12) and the original Zhang model is the addition of the exponent term, $(1 - 1/z)$. Since z is greater than 1, the exponent term must have a value between 0 and 1, which should reduce the rate at which TB spacing increases with respect to increasing SFE. By identifying and linking composition, SFE, and growth twinning trends, the model can be used to either validate

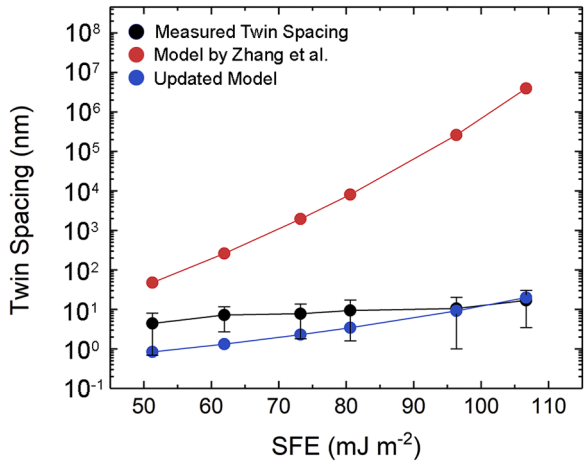

Fig. 5. Comparison of measured and predicted twin boundary spacings as a function of stacking fault energy (SFE). The black data points represent the measured twin spacings, while the predicted values for the Zhang model and updated model are shown by the red and blue points, respectively [4]. (For interpretation of the references to colour in this figure legend, the reader is referred to the web version of this article.)

experimentally determined and computationally predicted SFEs or to directly estimate SFEs using measured TB spacings. To demonstrate the applicability of the updated model, measured TB spacings were used in conjunction with MS estimated SFE's to determine the exponent term for the CuNi alloy system, which was calculated to be ~ 0.25. See supplementary materials for details regarding MS SFE calculations.

Fig. 5 analyzes the fit of the updated and original models by comparing their predicted TB spacings (calculated using the MS SFE values) with the experimentally observed values. TB spacing is plotted as a function of the SFE in mJ m^{-2}, where the Zhang model is shown by the red points, the updated model by the blue points, and the experimentally measured TB spacings by the black points. Here it can be observed that the predicted TB spacings from the previous model increase at an exponentially faster rate than the measured TB spacings from this study, while the updated model is in agreement with the experimentally observed values. The improved fit of the updated model supports its ability to directly predict and link growth TB formation with SFE and corroborates the assumption that the top surface energy of a "perfect" columnar grain affects growth twinning predictions. Thus, by having experimentally measured TB spacings and as few as two SFE values, the updated model can be used to predict nanotwin formation over an entire compositional space. The updated model was verified using previously published data on growth twin formation from other material systems with low SFEs, including single elements, binary alloys, and more complex engineering alloys, and a good fit was observed between the predicted and experimental values [4,28,31]. This highlights an improved fundamental understanding of growth twinning, which was obtained by using a CHT approach to globally evaluate growth NT formation.

4. Conclusion

In this work, NT formation in CuNi alloys was investigated using high-throughput experimental techniques in order to understand the fundamental relationships between growth twinning and both intrinsic and extrinsic material properties. Over 300 unique CuNi samples were synthesized via combinatorial sputtering. A comprehensive material library comprised of composition, hardness, crystallographic, and phase data was compiled using high-throughput characterization. This library highlighted the suitability of CuNi systems for probing growth NT formation, evidenced by the consistent texture, phase, and morphology across samples. The interrelationships among growth twinning, composition, and SFE, were examined by characterizing representative samples using STEM and ImageJ. Contrary to the existing growth twinning model, NT microstructures were observed in all compositional variations. Consequently, a revised model was developed using the NT data from this study, which can predict NT formation over entire composition spaces by accounting for all free energy contributions during nucleation. In summary, this work delineates a novel approach for examining growth twinning and other microstructural and intrinsic material phenomena using CHT techniques.

Declaration of competing interest

The authors declare that they have no known competing financial interests or personal relationships that could have appeared to influence the work reported in this paper.

Acknowledgements

This work was supported by the National Science Foundation (Grant Numbers: DMR-2227178 and OISE-2106597). Adie Alwen acknowledges fellowship support through the National Defense Science and Engineering Graduate (NDSEG) Fellowship Program, which is offered by the Department of Defense and sponsored by the Air Force Research Laboratory, the Office of Naval Research, and the Army Research Office. The authors acknowledge the Forschungszentrum Julich (FZJ), the Ersnt-Ruska Center (ERC), and the Core Center of Excellence in Nano Imaging (CNI) at the University of Southern California for access to their characterization facilities. The authors would also like to acknowledge Drs. Nico Peters and Mirko Ziegner from the FZJ for their assistance and helpful discussions.

Supplementary materials

Supplementary material associated with this article can be found, in the online version, at doi:10.1016/j.actamat.2024.119839.

References

[1] I.J. Beyerlein, X. Zhang, A. Misra, Growth twins and deformation twins in metals, Ann. Rev. Mater. Res. 44 (2014) 329–363, https://doi.org/10.1146/annurev-matsci-070813-113304.
[2] H. Gleiter, The formation of annealing twins, Acta Metall 17 (1969) 1421–1428, https://doi.org/10.1016/0001-6160(69)90004-2.
[3] S. Mahajan, D. Williams, Deformation twinning in metals and alloys, Int. Met. Rev. 18 (1973) 43–61, https://doi.org/10.1179/imtlr.1973.18.2.43.
[4] X. Zhang, A. Misra, H. Wang, T. Shen, M. Nastasi, T. Mitchell, J. Hirth, R. Hoagland, J. Embury, Enhanced hardening in Cu/330 stainless steel multilayers by nanoscale twinning, Acta Mater 52 (2004) 995–1002, https://doi.org/10.1016/j.actamat.2003.10.033.
[5] L. Lu, Y. Shen, X. Chen, L. Qian, K. Lu, Ultrahigh strength and high electrical conductivity in copper, Science 304 (2004) 422–426, https://doi.org/10.1126/science.1092905.
[6] O. Anderoglu, A. Misra, F. Ronning, H. Wang, X. Zhang, Significant enhancement of the strength-to-resistivity ratio by nanotwins in epitaxial Cu films, J. Appl. Phys. 106 (2009) 024313, https://doi.org/10.1063/1.3176483.
[7] K. Lu, L. Lu, S. Suresh, Strengthening materials by engineering coherent internal boundaries at the nanoscale, Science 324 (2009) 349–352, https://doi.org/10.1126/science.1159610.
[8] T.E.J. Edwards, N. Rohbeck, E. Huszár, K. Thomas, B. Putz, M.N. Polyakov, X. Maeder, L. Pethö, J. Michler, Thermally Stable Nanotwins: new Heights for Cu Mechanics, Adv. Sci 9 (2022) 2203544, https://doi.org/10.1002/advs.202203544.
[9] L. Velasco, A.M. Hodge, The mobility of growth twins synthesized by sputtering: tailoring the twin thickness, Acta Mater 109 (2016) 142–150, https://doi.org/10.1016/j.actamat.2016.02.042.
[10] P. Gallagher, The influence of alloying, temperature, and related effects on the stacking fault energy, Metall. Trans. 1 (1970) 2429–2461, https://doi.org/10.1007/BF03038370.
[11] R. Smallman, P. Dobson, Stacking fault energy measurement from diffusion, Metall. Trans. 1 (1970) 2383–2389, https://doi.org/10.1007/BF03038367.
[12] J. Christian, V. Vitek, Dislocations and stacking faults, Rep. Prog. Phys. 33 (1970) 307, https://doi.org/10.1088/0034-4885/33/1/307.
[13] P. Ferreira, P. Müllner, A thermodynamic model for the stacking-fault energy, Acta Mater 46 (1998) 4479–4484, https://doi.org/10.1016/S1359-6454(98)00155-4.

[14] W. Li, S. Lu, Q.M. Hu, S.K. Kwon, B. Johansson, L. Vitos, Generalized stacking fault energies of alloys, J. Phys. - Condens. Mat. 26 (2014) 265005, https://doi.org/10.1088/0953-8984/26/26/265005.

[15] J.A. Castañeda, O.A. Zambrano, G.A. Alcázar, S.A. Rodríguez, J.J. Coronado, Stacking fault energy determination in fe-mn-al-c austenitic steels by x-ray diffraction, Metals (Basel) 11 (2021) 1701, https://doi.org/10.3390/met11111701.

[16] G. Arora, D.S. Aidhy, Machine learning enabled prediction of stacking fault energies in concentrated alloys, Metals (Basel) 10 (2020) 1072, https://doi.org/10.3390/met10081072.

[17] X. Sun, S. Lu, R. Xie, X. An, W. Li, T. Zhang, C. Liang, X. Ding, Y. Wang, H. Zhang, Can experiment determine the stacking fault energy of metastable alloys? Mater. Des. 199 (2021) 109396 https://doi.org/10.1016/j.matdes.2020.109396.

[18] Y. Su, S. Xu, I.J. Beyerlein, Density functional theory calculations of generalized stacking fault energy surfaces for eight face-centered cubic transition metals, J. Appl. Phys. 126 (2019) 105112, https://doi.org/10.1063/1.5115282.

[19] R.D. Janani, S.A. Salman, K.P. Priyadharshini, V. Karthik, Effect of composition on the stacking fault energy of copper-nickel alloys using molecular dynamics simulations, Mater. Today-Proc 39 (2021) 1796–1800, https://doi.org/10.1016/j.matpr.2020.07.737.

[20] A. Ludwig, Discovery of new materials using combinatorial synthesis and high-throughput characterization of thin-film materials libraries combined with computational methods, NPJ Comput. Mater. 5 (2019) 70, https://doi.org/10.1038/s41524-019-0205-0.

[21] R. Potyrailo, K. Rajan, K. Stoewe, I. Takeuchi, B. Chisholm, H. Lam, Combinatorial and high-throughput screening of materials libraries: review of state of the art, ACS Comb. Sci. 13 (2011) 579–633, https://doi.org/10.1021/co200007w.

[22] S.A. Kube, S. Sohn, D. Uhl, A. Datye, A. Mehta, J. Schroers, Phase selection motifs in High Entropy Alloys revealed through combinatorial methods: large atomic size difference favors BCC over FCC, Acta Mater 166 (2019) 677–686, https://doi.org/10.1016/j.actamat.2019.01.023.

[23] K. Kim, S. Park, T. Kim, Y. Park, G.D. Sim, D. Lee, Mechanical, electrical properties and microstructures of combinatorial Ni-Mo-W alloy films, J. Alloy Compd. 919 (2022) 165808, https://doi.org/10.1016/j.jallcom.2022.165808.

[24] D.B. Miracle, M. Li, Z. Zhang, R. Mishra, K.M. Flores, Emerging capabilities for the high-throughput characterization of structural materials, Ann. Rev. Mater. Res. 51 (2021) 131–164, https://doi.org/10.1146/annurev-matsci-080619-022100.

[25] M.L. Green, I. Takeuchi, J.R. Hattrick-Simpers, Applications of high throughput (combinatorial) methodologies to electronic, magnetic, optical, and energy-related materials, J. Appl. Phys. 113 (2013) 231101, https://doi.org/10.1063/1.4803530.

[26] X. Zhang, Y. Xiang, Combinatorial approaches for high-throughput characterization of mechanical properties, J. Materiomics 3 (2017) 209–220, https://doi.org/10.1016/j.jmat.2017.07.002.

[27] D. Bufford, H. Wang, X. Zhang, High strength, epitaxial nanotwinned Ag films, Acta Mater 59 (2011) 93–101, https://doi.org/10.1016/j.actamat.2010.09.011.

[28] L. Velasco, M.N. Polyakov, A.M. Hodge, Influence of stacking fault energy on twin spacing of Cu and Cu–Al alloys, Scr. Mater. 83 (2014) 33–36, https://doi.org/10.1016/j.scriptamat.2014.04.002.

[29] G.M. Valentino, P.P. Shetty, A. Chauhan, J.A. Krogstad, T.P. Weihs, K.J. Hemker, Nanotwin formation in Ni–Mo–W alloys deposited by dc magnetron sputtering, Scr. Mater. 186 (2020) 247–252, https://doi.org/10.1016/j.scriptamat.2020.05.031.

[30] P. Uttam, V. Kumar, K.H. Kim, A. Deep, Nanotwinning: generation, properties, and application, Mater. Des. 192 (2020) 108752, https://doi.org/10.1016/j.matdes.2020.108752.

[31] R.T. Ott, J. Geng, M.F. Besser, M.J. Kramer, Y. Wang, E. Park, R. LeSar, A. King, Optimization of strength and ductility in nanotwinned ultra-fine grained Ag: twin density and grain orientations, Acta Mater 96 (2015) 378–389, https://doi.org/10.1016/j.actamat.2015.06.030.

[32] Z. Wang, C. Wang, Y.L. Zhao, Y.C. Hsu, C.L. Li, J.J. Kai, C.T. Liu, C.H. Hsueh, High hardness and fatigue resistance of CoCrFeMnNi high entropy alloy films with ultrahigh-density nanotwins, Int. J. Plasticity 131 (2020) 102726, https://doi.org/10.1016/j.ijplas.2020.102726.

[33] Y. Zhao, T.A. Furnish, M.E. Kassner, A.M. Hodge, Thermal stability of highly nanotwinned copper: the role of grain boundaries and texture, J. Mater. Res. 27 (2012) 3049–3057, https://doi.org/10.1557/jmr.2012.376.

[34] T. Furnish, A. Hodge, On the mechanical performance and deformation of nanotwinned Ag, APL Mater 2 (2014), https://doi.org/10.1063/1.4873215.

[35] K. Yu, D. Bufford, Y. Chen, Y. Liu, H. Wang, X. Zhang, Basic criteria for formation of growth twins in high stacking fault energy metals, Appl. Phys. Lett. 103 (2013) 181903, https://doi.org/10.1063/1.4826917.

[36] G. Pharr, W. Oliver, Measurement of thin film mechanical properties using nanoindentation, MRS Bull 17 (1992) 28–33, https://doi.org/10.1557/S0883769400041634.

[37] D. Tomus, H.P. Ng, In situ lift-out dedicated techniques using FIB–SEM system for TEM specimen preparation, Micron 44 (2013) 115–119, https://doi.org/10.1016/j.micron.2012.05.006.

[38] O.R. Deluigi, R.C. Pasianot, F. Valencia, A. Caro, D. Farkas, E.M. Bringa, Simulations of primary damage in a High Entropy Alloy: probing enhanced radiation resistance, Acta Mater 213 (2021) 116951, https://doi.org/10.1016/j.actamat.2021.116951.

[39] T. Gao, H. Song, B. Wang, Y. Gao, Y. Liu, Q. Xie, Q. Chen, Q. Xiao, Y. Liang, Molecular dynamics simulations of tensile response for FeNiCrCoCu high-entropy alloy with voids, Int. J. Mech. Sci. 237 (2023) 107800, https://doi.org/10.1016/j.ijmecsci.2022.107800.

[40] H. Xie, Z. Ma, W. Zhang, H. Zhao, L. Ren, Amorphization transformation in high-entropy alloy FeNiCrCoCu under shock compression, J. Mat. Sci. Technol. 175 (2024) 72–79, https://doi.org/10.1016/j.jmst.2023.07.049.

[41] D.Q. Doan, Effects of crystal orientation and twin boundary distance on mechanical properties of FeNiCrCoCu high-entropy alloy under nanoindentation, Mater. Chem. Phys. 291 (2022) 126725, https://doi.org/10.1016/j.matchemphys.2022.126725.

[42] A.P. Thompson, H.M. Aktulga, R. Berger, D.S. Bolintineanu, W.M. Brown, P. S. Crozier, P.J. in't Veld, A. Kohlmeyer, S.G. Moore, T.D. Nguyen, LAMMPS-a flexible simulation tool for particle-based materials modeling at the atomic, meso, and continuum scales, Comput. Phys. Commun. 271 (2022) 108171, https://doi.org/10.1016/j.cpc.2021.108171.

[43] A. Stukowski, Visualization and analysis of atomistic simulation data with OVITO–the Open Visualization Tool, Model. Simul. Mat. Sci. Eng. 18 (2009) 015012, https://doi.org/10.1088/0965-0393/18/1/015012.

[44] Z. Wang, D. Han, X. Li, Competitive effect of stacking fault energy and short-range clustering on the plastic deformation behavior of Cu-Ni alloys, Mater. Sci. Eng. A 679 (2017) 484–492, https://doi.org/10.1016/j.msea.2016.10.064.

[45] C. Carter, S. Holmes, The stacking-fault energy of nickel, Philos. Mag. 35 (1977) 1161–1172, https://doi.org/10.1080/14786437708232942.

[46] W.D. Callister, D.G. Rethwisch, Materials Science and Engineering: An Introduction, 9th ed., Wiley, Hoboken, New Jersey, 2014.

[47] T. Massalski, H. Okamoto, P.R. Subramanian, L. Kacprzak, Binary Alloy Phase Diagrams, 2nd ed., ASM International, Materials Park, OH, 1990.

[48] W. Soboyejo, Mechanical Properties of Engineered Materials, 1st ed., CRC press, 2002.

[49] J. Weertman, Hall-Petch strengthening in nanocrystalline metals, Mater. Sci. Eng. A 166 (1993) 161–167, https://doi.org/10.1016/0921-5093(93)90319-A.

[50] B.J. Lee, J.H. Shim, M. Baskes, Semiempirical atomic potentials for the fcc metals Cu, Ag, Au, Ni, Pd, Pt, Al, and Pb based on first and second nearest-neighbor modified embedded atom method, Phys. Rev. B 68 (2003) 144112, https://doi.org/10.1103/PhysRevB.68.144112.

[51] D. Udler, D. Seidman, Grain boundary and surface energies of fcc metals, Phys. Rev. B 54 (1996) R11133, https://doi.org/10.1103/PhysRevB.54.R11133.